4 Thermal and Geometrical Effects on Bulk Permittivity of Porous Mixtures Containing Bound Water

Scott B. Jones and Dani Or

Department of Plants, Soils, and Biometeorology; Utah State University; Logan, UT, USA, 84322-4820 and Department of Civil and Environmental Engineering; University of Connecticut; Storrs, CT, USA, 06269-2037

4.1 Introduction

Determination of the water content of porous media (e.g., soil, powders, cereal grains) from measured bulk dielectric, ε_b, is based on the dominance of the high dielectric permittivity of liquid water relative to that of solids and air. Dielectric measurements in many minerals comprising soils for example, exhibit behavior described by a general empirical relationship [1], while measurements in high surface area materials or in particles of high aspect ratio exhibit unique and varied dielectric-water content relationships. Factors contributing to the unique dielectric-water content relation of certain porous media include water binding and dipole interactions that arise from particle geometry and water-phase configuration in addition to measurement frequency and dielectric loss. Thermal perturbation of high surface area porous media demonstrates strong interactions between bound and free water that have been shown to produce either an increase or decrease in bulk dielectric for a fixed water content. This effect is demonstrated by modeling the dielectric permittivity of bound and free water-phases, where the surface area-dependent bound water film thickness and the temperature-dependent permittivity of free water are combined. The water-phase permittivity is the least well-defined constituent and yet the most critical for predicting the bulk permittivity of a three-phase water-, solid- and air-system. A three-phase dielectric mixture model is shown to provide a physically-based approach for modeling porous media permittivity. Phase configuration in addition to estimates of particle and packing densities facilitate volume tracking with water content change.

4.1.1 Dielectric Mixing Theory

A dielectric mixture may be described in terms of the volume fractions and dielectric permittivities of constituents. A host of different mixture models have been developed for multiple phases using different methods of homogenization, including variations on constituent geometry leading to isotropic and anisotropic

mixtures and combinations thereof [2]. We approximate a porous mixture as a two- or three-phase system made up of solids, water and air. The confocal ellipsoid model shown in Fig. 4.1 is an example of such a three-phase system and serves as a geometrical basis for a unit cell leading to an approximate porous mixture. We assign water-, solid- and air-phase permittivities ε_w (80), ε_a (1), ε_s (5) and volumetric fractions ϕ_w, ϕ_a, and ϕ_s, respectively [3]. As we will demonstrate later, ε_w will be subject to temperature and relaxation effects requiring further attention for improved modeling. Constituent volume fractions are related through measurable quantities of dry bulk density (ρ_b = dry solid mass per bulk volume) and solid particle density (ρ_s = solid mass per solid volume) from which we obtain total (bulk) porosity (ϕ_b), which describes the fluid-filled portion of the mixture (i.e., $\phi_b = 1 - \rho_b/\rho_s$). The air ($\phi_a$) and solid ($\phi_s$) fractions may be described as $\phi_a = \phi_b - \phi_w$ and $\phi_s = 1 - \phi_b$, respectively. Dielectric mixture theory offers the advantage of physically-based predictions of bulk permittivity based on constituent permittivities and their volumetric contributions to the mixture [4]. Predicting the dielectric permittivities of constituents in high surface area materials is complicated by the presence of bound water.

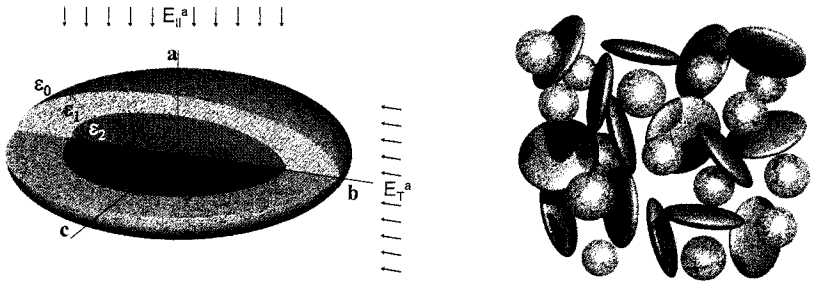

Fig. 4.1. On the *left*, a three-phase unit cell described as a confocal spheroid (core, ε_2, and shell, ε_1) contained in a background, ε_0. The orientation of the electric field ($\mathbf{E}$) is either normal (E_T^a) or parallel ($E_{\|}^a$) with respect to the rotation axis, *a*, of the spheroid. On the *right*, a random mixture of spheroids forms an idealized porous medium

4.1.2 Geometrical Effects

Particle shape may influence electromagnetic measurements, depending on the particle geometry and orientation (random, aligned) with respect to the applied electrical field [5] as illustrated in Fig. 4.1. The shape of soil particles or portions of cereal grains from the kernel itself, to the starch granule, to the molecular components, influence the dielectric measurement due to the dipole moment each component imposes in an electromagnetic measurement of permittivity. Aspect ratio is a common descriptor for geometry, and those of clay minerals can be extreme in comparison to nearly spherical sand grains. Minimum and maximum aspect ratios for several clays are listed in Table 4.1, given based on estimates of

particle planar diameter and thickness. Aspect ratios for three common cereal grains are also listed. Particle shape effects have been measured on individual kernels [6] and on mixtures of isotropic [7-9] and anisotropic particles [5].

Table 4.1. Dimensions and aspect ratios of certain clay minerals and cereal grain kernels.

Clay mineral†	Thickness, *a* [nm]	Diameter, *b* [μm]	Minimum *a/b*	Maximum *a/b*
Kaolinite	50	0.1 – 4	0.5	0.0125
Chlorite	10 – 100	0.1 – 2	1	0.005
Illite	5 – 30	0.1 – 2	0.3	0.0025
Montmorillonite	1 – 10	0.01 – 1	1	0.001
Kernel‡	**Length, *a* [mm]**	**Width, *b* [mm]**	**Minimum *a/b***	**Maximum *a/b***
Corn	8 – 17	5 – 15	0.5	3.4
Rice	5 – 10	1.5 – 5	1	6.7
Wheat	5 – 8	2.5 – 4.5	1.1	3.2

†[10], ‡[11].

4.1.3 Bound Water

Water that is "bound" to solid surfaces is subject to surface forces that hinder its response to an imposed electromagnetic field, resulting in both a lower relaxation frequency and in lower ε_b relative to free liquid water.

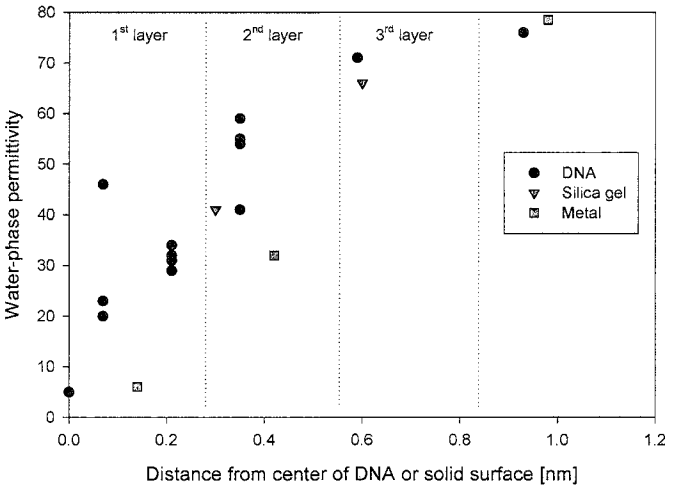

Fig. 4.2. Water-phase permittivities computed as a function of distance from the center of DNA [12] and measured thickness on the surface of silica gel [13] and metal [14]. The mono-layer water thickness is assumed to be 0.28 nm

The first monolayer of bound water closest to the solid surface is held most tightly and has the lowest measured ε_b. The bulk permittivity of successive molecular water layers increases with distance from the solid surface up to that of free water at around 3 or more molecular layers (see Fig. 4.2). The dielectric permittivity of wet materials, high surface area, (i.e., clays, peats, starches, proteins, etc.) exhibit reduced bulk dielectric permittivities compared to materials with lower surface areas at the same volumetric water content as a result of bound water and shape effects. The large surface area of minerals is often associated with plate- or needle-like particles of high aspect ratio as shown in Table 1. Assuming disk-shaped geometries, specific surface areas range from 15 to 750 $m^2\ g^{-1}$ for Kaolinite and Montorillonite, respectively. In the case of biological materials, the molecular structure is much more complex but capable of similarly large specific surface areas, only a portion of which are generally water accessible.

4.2 Theoretical Considerations

Modeling the dielectric behavior of a complex porous mixture is generally approached using a simplified representation of constituents, configurations and geometries, all of which play a role in the bulk dielectric. Here we briefly consider models describing the water–phase, the influence of shape and the configuration of constituent phases.

4.2.1 Water-Phase Permittivity

Water molecules are subject to thermal and interfacial effects that can create significant changes in the water-phase permittivity with changes in temperature and measurement frequency. In addition, the specific surface area of the solid-phase is proportional to the amount of water bound within a porous medium. Air and most solid materials, unlike water, show little change in permittivity with changes in temperature or frequency [15, 16]. In the following we will discuss water as "free" molecules in bulk water or as "bound" molecules that are hindered to some extent in their movement or rotation. The effects of temperature on the permittivity of free and bound water will also be discussed.

Free Water

A water molecule possesses both a permanent dipole moment, resulting from the structure and charges of its atomic components, and a polarizability component that is in proportion to the magnitude of an applied electric field. In the presence of strong electric fields, the polarizability component may actually reduce the dielectric permittivity of water significantly [17]. In the presence of a mild alternating electric field, water molecules exhibit dielectric dispersion leading to a frequency dependent real component of permittivity that is reduced as frequency increases. This

phenomenon results from the molecules' inability to reorient in response to the changing electric field. As a consequence, the permittivity contribution of the permanent dipole orientation is diminished and eventually lost at higher frequencies. The reduction in the real permittivity component shows up in the imaginary or 'loss' component, which for free water arises in the GHz frequency band, where a phase lag develops between the applied electric field and the dipole orientation. This effect draws energy from the electric source that is dissipated as heat. For water molecules whose motion is hindered by the attractive forces of solid surfaces and adjacent molecular forces (other than neighboring free water molecules), their relaxation frequency may be reduced to within the MHz frequency range.

Permittivity measurement instruments vary both in their application (for measuring liquid, solid or gas) and in their frequency measurement range. Time domain reflectometry (TDR) instruments, for example, exhibit a frequency bandwidth, f_b, which is largely determined by the rise time (t_r) of the instrument. Instrument rise times commonly employed in soil sciences vary from 125 to 300 ps [18] corresponding to frequency bandwidths of 2.8 to 1.2 MHz, respectively (e.g., $f_b = \ln(0.9/0.1)/(2\pi t_r) \sim 0.35/t_r$ [19]). Lower frequency capacitive measurement instruments may have much lower measurement frequencies in the MHz range.

Bound Water

The influence of water binding on permittivity reduction has been measured [12-14]. The water-phase permittivity associated with attachment to different solid materials is illustrated in Fig. 4.2, where increased water layer thickness leads to an increase in permittivity. These measurements are more difficult to make than free liquid measurements owing to the molecular scale at which they occur and to differing measurement methods. It is understood that the mechanism causing the permittivity reduction is related to the hindered rotation of the water molecules in the vicinity of solid surfaces. Less well understood is the character of the bound water, its density and packing arrangement.

4.2.2 Water-Phase Temperature-Dependence

The temperature dependence of the dielectric permittivity of porous materials can be attributed largely to the effect of temperature on the water-phase. The temperature dependent permittivity of free water is described by the following expression [20].

$$\begin{aligned}\varepsilon_{fw}(T) = 78.54[1 - 4.579x10^{-3}(T-298) \\ +1.19x10^{-5}(T-298)^2 - 2.8x10^{-8}(T-298)^3]\end{aligned} \tag{4.1}$$

where T [K] is the temperature. The temperature dependence of the bound portion of water is more complicated, especially since the boundary between bound and free water is vague. Or and Wraith [21] derived a temperature-dependent model describing bound water content (M_{bw}), expressed in terms of the bound water layer

thickness, x(T) [m], the specific surface area, A_s [m^2 g^{-1}], and the bulk density, ρ_b [g m^{-3}], of the porous medium, written as

$$M_{bw} = x(T) \cdot A_S \cdot \rho_b \tag{4.2}$$

where x(T) was derived from the viscosity profile of water as a function of distance from a clay surface coupled with the Debye [22] model predicting relaxation frequency of a polar liquid. Or and Wraith have used a cutoff frequency, f^* [Hz], below which bound water relaxes and thus practically does not affect a TDR signal. The resulting temperature-dependent bound water layer thickness, x(T) [m], is computed as

$$x(T) = \frac{a}{-d + T \cdot \ln\left(\dfrac{k \cdot T}{8\pi^2 r^3 c \cdot f_{rel}}\right)} \tag{4.3}$$

where the constants α = 1621 [Å K], d = 2.047 x 10^3 [K], c = 9.5 x 10^{-7} [Pa s], k is the Boltzman constant (1.38062 x 10^{-23} [J K^{-1}]) and r [m] is the radius of the bound water molecule (~ 1.8 - 2.5 Å).

4.2.3 Particle Shape Effects

The depolarization factor accounts for the dipole effect arising from the particle shape-field alignment, which influences the measured bulk permittivity. The exact solution to the depolarization factor given by Landau and Lifshitz [23] is written in terms of field-axis orientation (e.g., N^a = E = field parallel to a in Fig. 4.1)

$$N^i = \int_0^\infty \frac{(abc)du}{2(u+i^2)\sqrt{(u+a^2)(u+b^2)(u+c^2)}} \qquad i = a,b,c \tag{4.4}$$

where N^a+N^b+N^c = 1 and u is a scalar. Equation (4.4) was parameterized in terms of a spheroid ($b = c$) using the aspect ratio (a/b) ranging from a disk- (a/b = 0.001) to a needle-shape (a/b = 1000) [5]. The resulting depolarization factor-aspect ratio relation was defined using the following empirical expression for parallel and normal and E-field alignment with respect to a spheroid's rotation axis.

$$N^p = \frac{1}{1 + 1.6\left(\dfrac{a}{b}\right) + 0.4\left(\dfrac{a}{b}\right)^2} \qquad N^n = \frac{1 - N^p}{2} \tag{4.5}$$

where the depolarization factor for the electrical field aligned parallel to the axis of symmetry (rotation axis) is N^p and is N^n when normal to the axis of symmetry (see Fig. 4.1).

4.2.4 Three-Phase Dielectric Mixture Model

Modeling the bulk permittivity of a three-phase system consisting of inclusions comprised of a core and outer shell of confocal ellipsoids (Fig. 4.1) allows accounting for particle shape effects via the depolarization factor in addition to phase configuration effects. The core, ε_2, and the outer shell, ε_1, are contained in a background host medium of permittivity, ε_0. The effective permittivity of an isotropic three-phase confocal system of ellipsoids may be written as [4],

$$\varepsilon_b = \varepsilon_0 + \frac{\frac{\varepsilon_0}{3}\sum_{i=p,n,n}\left(\frac{n_v\alpha^i}{\varepsilon_0}\right)}{1-\frac{1}{3}\sum_{i=p,n,n}N_1^i\left(\frac{n_v\alpha^i}{\varepsilon_0}\right)} \tag{4.6}$$

where the polarizability term in parenthesis is given as a series expansion written here for the dual, confocal ellipsoid system as

$$\frac{n_v\alpha^i}{\varepsilon_0} = (\phi_1+\phi_2)\cdot \left[\frac{(\varepsilon_1-\varepsilon_0)+\left[\varepsilon_1+N_1^i(\varepsilon_0-\varepsilon_1)\right]\cdot\frac{(\varepsilon_2-\varepsilon_1)\frac{\phi_2}{(\phi_1+\phi_2)}}{\left[\varepsilon_1+N_2^i(\varepsilon_2-\varepsilon_1)\right]}}{\left[\varepsilon_0+N_1^i(\varepsilon_1-\varepsilon_0)\right]+N_1^i(1-N_1^i)(\varepsilon_1-\varepsilon_0)\cdot\frac{(\varepsilon_2-\varepsilon_1)\frac{\phi_2}{(\phi_1+\phi_2)}}{\left[\varepsilon_1+N_2^i(\varepsilon_2-\varepsilon_1)\right]}}\right] \tag{4.7}$$

where ϕ_1 and ϕ_2 are the volumetric fractions and N_1^i and N_2^i are the depolarization factors of the shell and core ellipsoids, respectively. Various combinations of solid, liquid- and gas-phases may be assigned to the core, shell and background.

4.3 Measurements and Modeled Results

For a fixed volume fraction of water the measured bulk dielectric can be significantly different for different porous mixtures. Possible contributors to these differences are discussed here and models for describing these effects are presented, including the interplay between bound and free water, geometrical effects, specific surface area related to water binding, porosity and density and phase configuration.

4.3.1 Permittivity Measurements in Porous Mixtures

The permittivity of porous mixtures has been described using empirical relationships such as those shown in Fig. 4.3. The Topp et al. [1] equation has been widely used to describe the permittivity of mineral soils measured using TDR. The empirical relationship given by Schaap et al. [24] was fitted to measured permittivities of forest soils. The differences between these two models can be attributed to several effects, including bound water present in porous media having high surface area, effects due to particle geometry, and the configuration of the water-phase [25]. A mineral soil and a pure clay mineral from Dirksen and Dasberg [26] are well described by these two models.

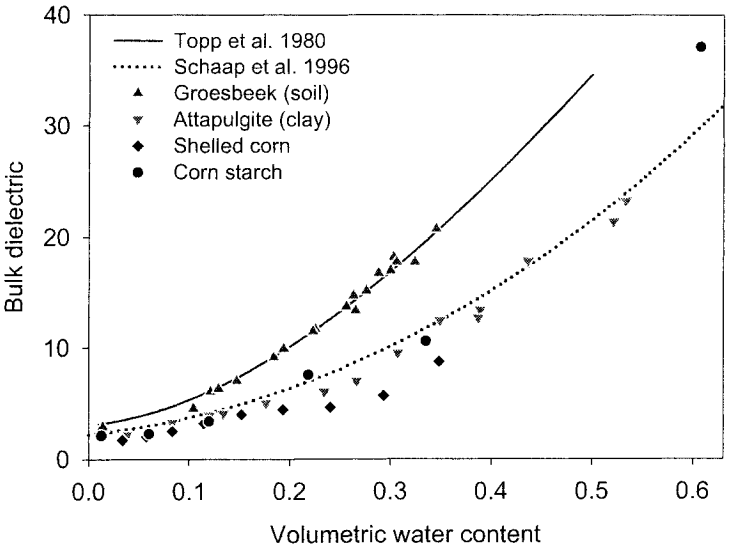

Fig. 4.3. Measured and modeled permittivities as a function of volumetric water content in different porous media. Groesbeek and Attapulgite data are from Dirksen and Dasberg (1993), the kernel and starch data were taken from Jones and Or (2002). The Topp et al. (1980) relation describes a wide range of mineral soils. The Schaap et al. (1996) model describes the permittivity of forest litter

4.3.2 Thermal Effects of Bound Water

The thermodielectric effect on the bulk permittivity of water within soil was suggested by Or and Wraith (1999) to be the result of an interplay between 1) the reduction in the permittivity of free water with increasing temperature, and 2) the increased permittivity brought about by the liberation of bound water to a less hindered state (i.e., greater permittivity illustrated in Fig. 4.4). They modeled this effect using Eq. (4.3) to represent the bound water influence on the bulk dielectric

constant of sand and clay mixtures illustrated in Fig. 4.4. They found an apparent lag in the temperature response and suggested a possible correction for this effect. Surface area was also back calculated by optimizing the thermodielectric effect on permittivity measurements.

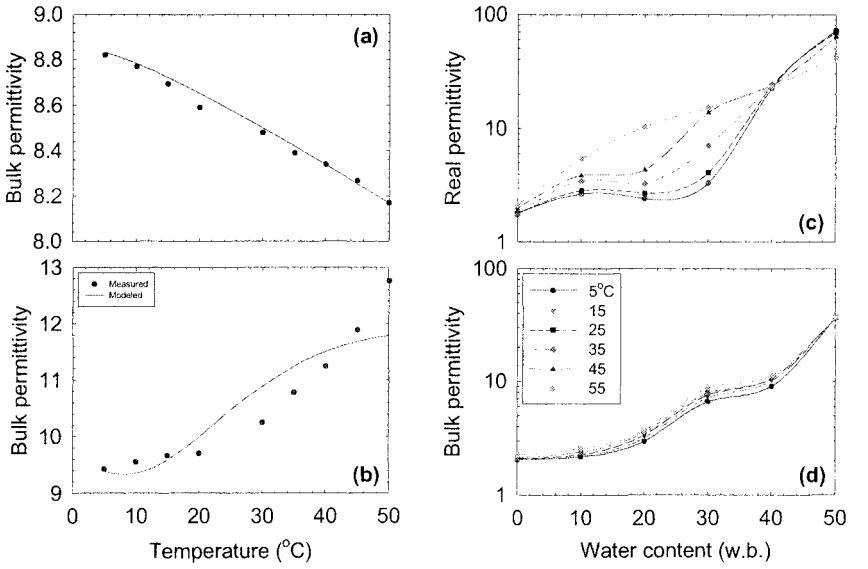

Fig. 4.4. The thermodielectric effect is illustrated in (a) for fine sand and in (b) for a sand-montmorillonite clay mixture, each at 15 % mass water content. Dominance of the opposing temperature dependence of bulk water in (a) for low surface areas, and bound water in (b) for high surface areas is demonstrated [21]. The thermodielectric effect is illustrated differently by permittivity measurements in corn starch using (c) at network analyzer at 500 MHz and (d) a time domain reflectometer [25].

The thermodielectric effect is further illustrated by bulk permittivity measurements in cornstarch shown in Fig. 4.4 and in other studies [27]. Network analyzer measurements (Fig. 4.4c) reveal a cross-over in the permittivity-temperature relationship with increasing water content at about 40 percent (wet basis) measured at a frequency of 500 MHz. TDR measured permittivities (Fig. 4.4d) also demonstrate the effect of bound water 'release' throughout the measured water content range up to 50 percent. The reversal in the temperature-permittivity trend occurring at higher water contents happens when starch granules approach water saturation, leading to a buildup of "free" water within and eventually between granules. Near saturation, temperature increase leads to reduced permittivity of the starch, similar to the reduction in free water permittivity with increasing temperature (Eq. (4.1)). The large permittivity differences at mid range moisture contents suggest an abundance of bound water which is liberated upon heating, and the nonlinear nature of the starch permittivity increase with added water also suggests an

evolution of the surface area with wetting or drying. Configuration of the water associated with solids combined with surface area evolution leading to changes in bound water fraction were suggested by [25] to cause the distinct plateau in the permittivity-water content curve shown in Fig. 4.4d for corn starch, and also noted in whole corn kernel measurements [28].

4.3.3 Modeling the Total Water-Phase Permittivity

Combining the temperature-dependent water-phase permittivity of bound and free water allows the use of a three-phase mixing model with shape effects. The bound water temperature-dependent expression, x(T) (Eq. (4.3)), was coupled with Eq. (4.1), following an exponential increase in permittivity with water layer thickness, t_w, resulting in the following expression

$$\varepsilon_w(T) = \varepsilon_{fw}(T) \cdot \left[1 - \exp\left(\frac{-t_w}{x(T)}\right)\right] \tag{4.8}$$

where t_w [m] can be calculated with M_v where $t_w = M_v/(A_s\,\rho_b)$. Computed temperature-dependent free water and bound water-phase permittivities are shown in Fig. 4.5. The temperature effect is presented in Fig. 4.5a where the free water permittivity, ε_{fw}, at 5 and 25°C is illustrated by a reduction in the water-phase permittivity. In Fig. 4.5a the temperature increase from 5 to 25°C is described by the reduction of x(T) releasing bound water to a more rotational state, which results in a higher effective permittivity. The free water permittivity is reduced with increa-sing temperature. The second phenomenon is the apparent 'release' of bound water from a lower to a higher rotational state, which occurs with increasing temperature. This bound water effect is illustrated in Fig. 4.5a by a reduction in the bound water layer thickness, x(T) with increasing temperature. In Fig. 4.5b these compe-ting phenomena are illustrated as the total water-phase permittivity plotted using Eq. (4.8) ($r = 2.5\times10^{-10}$, $A_s = 400$ m^2 g^{-1}, $f^* = 1$ GHz) and demonstrating the thermodielectric behavior as a function of water content Predicted permittivities in Fig. 4.5b are generally correlated to measurements in silica gel, metal powder and DNA shown in Fig. 4.2 and to temperature dependent measurements shown in Fig. 4.4. From Fig. 4.2 the average of the measured and simulated dielectric permittivities for mono-molecular layers 1, 2, and 3, are 27, 47, and 69 while corresponding modeled values (T = 25°C in Fig. 4.5) are 22, 49, and 63, respectively.

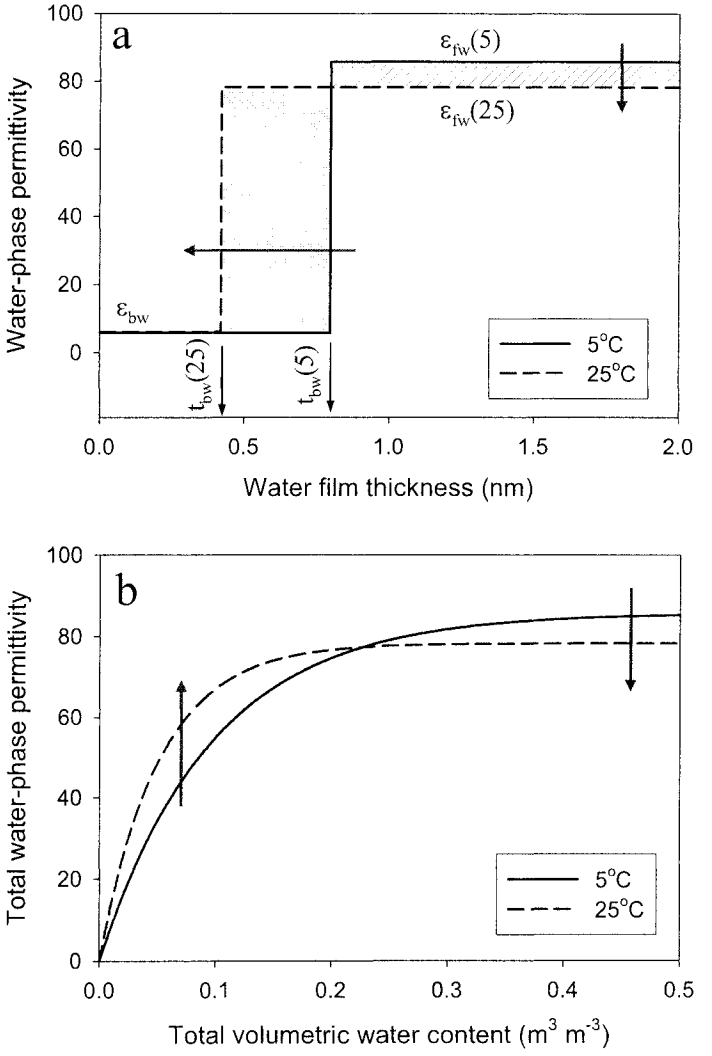

Fig. 4.5. Illustration of the thermodielectric effect described in **a)** by the temperature-dependent responses of reduced free water-phase permittivity (ε_{fw}) with increasing temperature and a reduced bound water layer thickness (x(T)). In **b)** these competing phenomena are illustrated as the total water-phase permittivity

4.3.4 Modeling Geometrical Effects

Particle shape effects influencing the dielectric permittivity of particulate mixtures may occur throughout a hierarchy of shapes and scales. In cereal grains, for example, this scale extends from the kernel to the starch grains and their complex internal structure, which extends down to the long chain and clustered polymers of amylose and amylopectin. In such complex structures the influence of shape on permittivity is difficult to determine. Effects of shape have been measured (using TDR) and modeled in simple systems using anisotropic packings of mica flakes where bound water is negligible [5].

Figure 4.6 illustrates measured permittivities in 0.25 mm diameter mica particles that were generally correlated to model predictions based on particle aspect ratio (geometry) and electrical field alignment as determined by probe orientation. Using Eqs. (4.5–7) and a combination of phase configurations the wet mica permittivity was modeled using an average aspect ratio of 1/25 and a porosity of 0.8. At mid- range water contents, measured data of $\varepsilon_{\text{eff}}^{a}$ is approximately half of the $\varepsilon_{\text{eff}}^{b}$ measurements. The measured permittivity of glass beads (inset) using the same system shows only a mild effect from the TDR probe (E-field) orientation. Reduced permittivity measurements in high surface area materials (e.g., clays) have been typically attributed to bound water effects. The reduction in permittivity in mica, which have very low specific surface area ($A_s < 0.06$ m^2 g^{-1}), should be attributed primarily to geometrical effects arising from the depolarizing influence of these high aspect ratio ($a/b = 1/25$) particles.

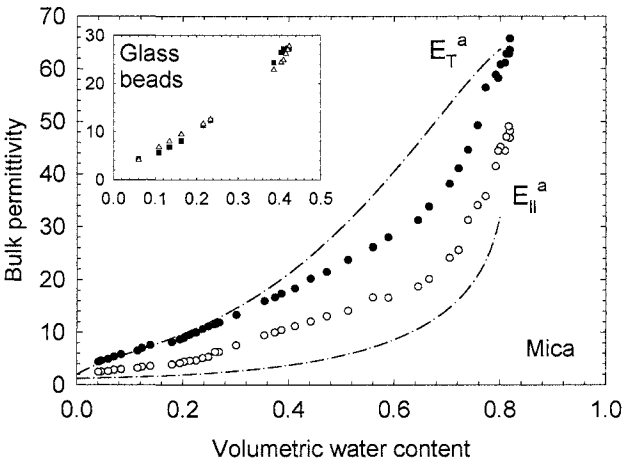

Fig. 4.6. Time domain reflectometry (TDR) measured bulk permittivity of partially saturated mica (0.25 mm diameter) and glass beads (inset). The orientation of the electric field (E) is described in Fig. 4.1 as being either normal (E_T^a) or parallel (E_{II}^a) with respect to the rotation axis, *a*, of the mica particle assumed oblate and layered horizontally [5]

Although the binding of water is well correlated to A_s, measuring or estimating specific surface area is generally not as simple as calculating A_s based on well defined particle geometry in the simplified mica system.

Specific Surface Area Determination

Specific surface area, A_s, of a porous medium can be defined as the total surface area of solid constituents per unit mass and is intimately tied to the sizes of particles and to their shape. For example, rounded sand particles may exhibit values of A_s from 1 to 10 $m^2\ g^{-1}$ while plate-like clay particles may yield a specific surface area ranging from 100 to 1000 $m^2\ g^{-1}$. This fundamental property of soils is correlated to important phenomena such as cation exchange, adsorption and release of chemicals, swelling, water retention and conductivity in addition to mechanical properties. Adsorption techniques are typically used to measure A_s directly [29]. Knowledge of particle size and geometry allows estimation of A_s using geometrical calculations of surface area. Another approach is based on the air-dried or hygroscopic water content, θ_h, (volume basis) as suggested by Robinson et al. [30]. They reported a linear correlation for A_s [$m^2\ g^{-1}$] as a function of θ_h that resulted from fitting data of 42 soils, given as

$$A_s = 35.7 \cdot \theta_h \tag{4.9}$$

Various techniques have been used to determine water binding in biological materials using measurement techniques including calorimetery, dilatometry, nuclear magnetic resonance, electron spin resonance, thermally stimulated depolarization currents, and others [31, 32]. Estimating specific surface area of the kernel or starch grain may be derived from the measured mono-layered water content and an estimate of the density of the mono-layered bound water. The assumed structure of the water molecules will also influence the estimate slightly. Ryden [33] suggested a relationship for water molecule spacing, s [Å], based on water density, ρ_w [g cm^{-3}], and packing given by

$$s = \sqrt[3]{\frac{K_p}{\rho_w}} \tag{4.10}$$

where K_p is a packing constant given as 28.21 [g $Å^3$ cm^{-3}] for tetrahedral and 29.92 [g $Å^3$ cm^{-3}] for cubic packings. Assuming a water density of 1 g cm^{-3}, the resulting water molecular spacing is 3.04 Å and 3.10 Å for tetrahedral and cubic packings, respectively. These values are representative of the intermolecular spacing of free water [34]. For bound water, however, two contrasting views have been presented. One suggests that the density of water is less than the density of free water [35, 36] leading to larger spacing between water molecules. Reduced densities were suggested to arise from inter lattice spacing constraints between clay platelets which were numerically simulated, producing fluid densities both greater

than and less than free water density depending on platelet separation [37]. For cereal grain constituents of protein and carbohydrate molecules, it is also conceivable that for certain structural spacing within and between molecules, reduced water densities are achievable.

Another view suggests water densities greater than that of free water [38-40], which correspond to a reduced water molecular spacing. Gur-Arieh et al. (1967) showed a constant wet flour density for moisture contents (w.b.) from 0 to 0.07 g g^{-1}, after which the wet density decreased steadily up to the final measured moisture content of 0.26. From this result they calculated a mono-layer water density, ρ_{ml}, of 1.48 g cm^{-3} and a density of the second molecular layer of water to be 1.11 g cm^{-3}. The remaining water layers were calculated to have a density of 0.967 g cm^{-3}. For a tetrahedral packing and using a mono-layer water density of 1.48 g cm^{-3} and a second layer density of 1.11 g cm^{-3}, Eq. (4.10) gives molecular spacing of 2.67 and 2.94 Å, respectively. These estimates lie on either side of spacing found in ice (hexagonal) of 2.76 Å (Robinson and Stokes, 1959) and are similar to other estimates of bound water spacing of between 2.5 Å and 2.8 Å [41]. For mono-layered water content given on a dry basis, M_{ml}, an estimate of the specific surface area, A_s [m^2 g^{-1}], is given using the estimated mono-layer water density, ρ_w [g cm^{-3}], and packing constant, K_p (Eq. (4.10)), given by

$$A_s = \frac{M_{ml}}{\rho_{ml} \cdot K_p^{1/3}} \tag{4.11}$$

Estimates based on this approach suggest A_s values of from several hundred to one thousand m^2 g^{-1} for starches and flours [32, 42, 43].

4.3.5 Modeling Porosity and Density

The physical make-up of porous mixtures is complicated by variations in texture and structure varying in size and shape. Particle geometry may take any number of forms from being plate-like to cylindrical or fiber-like to granular or blocky. Examples are found in soils where aspect ratios of certain clays (a/b = 0.033-0.025 [44]) and mica particles (a/b = 0.04, [5]) are extreme examples of oblate shapes (See Table 1). Many soil particles are generally spherical like sands (a/b = 0.46) or Tuff (a/b = 0.35) [9]. Prolate shapes are found in minerals such as hematite (a/b = 3.4, [45]) or fibers of peat (a/b = 10 to 100). As mentioned earlier, such shapes are often approximated using ellipsoidal or spheroidal geometries. From such approximations, physical characteristics of volume and surface area may be calculated. For porous mixtures comprised of spheroidal particles, an approximation of bulk porosity, ϕ_b, references the ratio of the representative particle volume to surface area [46]

$$\phi_b = 1 - k\frac{V_p^{\frac{2}{3}}}{S_p} \tag{4.12}$$

where k is an empirical scaling coefficient, V_p is the volume of the particle and S_p is the individual particle external surface area. The dimensionless volume to surface area ratio, $V_p^{2/3}/S_p$, forms a unique relationship for a spheroidal geometry and varying aspect ratio. Using approximate relationships for a spheroid of unit volume whose surface area [5] varies with aspect ratios (a/b) from 0.001 to 1000, the following empirical expression was obtained

$$\frac{V_p^{2/3}}{S_p} = \left[4.53 + 0.671 \left(\ln \frac{a}{b} \right)^2 + 0.309 \left(\frac{b}{a} \right) \right]^{-1} \tag{4.13}$$

Modeled porosities as functions of aspect ratio are plotted using Eqs. (4.12) ($k = 3$) and (4.13). The volume-surface-area relationship reproduces the general trend of increased porosity as aspect ratio deviates from that of a sphere ($a/b = 1$) for either oblate or prolate shapes. Comparison to measured or computed bulk porosities in a variety of porous media suggest these relationships provide reasonable predictions of bulk porosity illustrated in Fig. 4.7. The fitting parameter, k, simply provides vertical scaling of the curve.

Next to water content, bulk density of the porous medium is among the most varied and critical factors affecting the permittivity measurement. Bulk density is directly related to the bulk porosity through the density of solids, ρ_s, in a given volume of porous media. This relationship is of a similar form to that in Eq. (4.12) and is written as

$$\phi_b = 1 - \frac{\rho_b}{\rho_s} \tag{4.14}$$

For shrinking or swelling materials such as cereal grains or clayey soils, ρ_b varies with water content and therefore the determination of bulk density is coupled to water content determination. For cereal grains, especially, the water contained within the grain may be directly tied to the change in kernel density, which is related to a commensurate change in ρ_b. This is illustrated using an expression relating the dry solid density, ρ_s, density of water, ρ_w, and the wet basis moisture content, M_{wb}, to the kernel density, ρ_k, written as [47]

$$\rho_k = \frac{\rho_s}{1 + \left(\frac{\rho_s}{\rho_w} - 1 \right) M_{wb}} \tag{4.15}$$

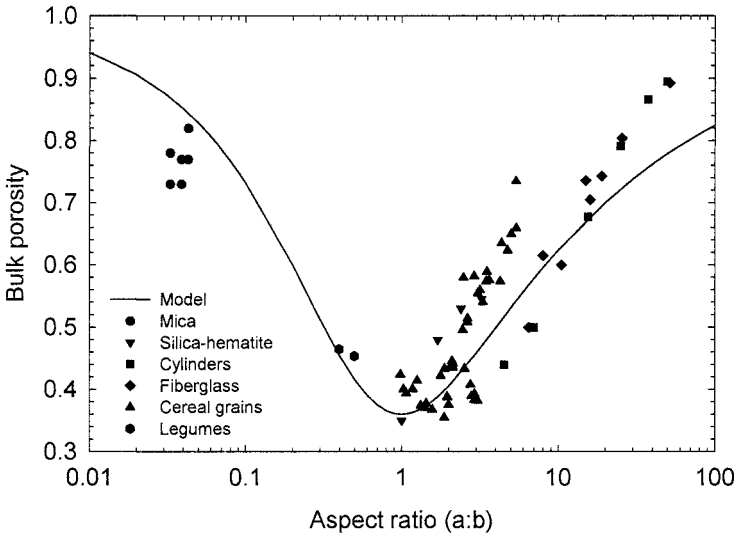

Fig. 4.7. Modeled bulk porosity of random packings of uniform spheroids as a function of particle aspect ratio. Data shown are measured porosities in (not necessarily randomly packed) mica particles [5], silica-hematite prolates [45], wooden cylinders and fiberglass rods [48], a variety of cereal grains [49], and legumes [50]

This simple expression requires only the dry solid density as a fitting parameter. For bulk density of the kernels, we consider the effect of kernel shape on packing by combining Eqs. (4.13) and (4.12) and setting them equal to Eq. (4.14) to solve in terms of bulk density. Note that for the bulk packing calculation, the solid density in Eq. (4.14) is assumed equal to the kernel density and Eq. (4.15) is substituted for ρ_s yielding

$$\rho_b = \frac{k \cdot \rho_s}{\left(4.53 + 0.671\left(\ln\frac{a}{b}\right)^2 + 0.309\left(\frac{b}{a}\right)\right)\cdot\left(1 + \left(\frac{\rho_s}{\rho_w} - 1\right)\cdot M_{wb}\right)} \tag{4.16}$$

This expression contains effects of the additional porosity and packing going from the kernel to the bulk packing. These two models are plotted in Fig. 4.8 compared to measured kernel and bulk densities in yellow-dent field corn.

Inverse bounds on constituent volume fractions derived from complex permittivity measurements and evaluation of the structural moments and geometry [51] may provide improved measurement capability where bulk density or porosity is often an unknown and confounding factor for water content determination. Furthermore, recent work using free-space measurements of complex permittivity at

GHz frequencies in cereal grains demonstrates the potential for density-independent measurements of moisture content [52].

To summarize geometrical effects, the specific surface area is a critical parameter used to estimate bound water content in porous media. Particle shape and particle density directly affect the specific surface area, packing and arrangement of the bulk mixture and can be used to compute estimates of A_s, ρ_b and ϕ_b. Each of these characteristics plays an important role in dielectric measurements for water content determination. These parameters can be employed in modeling permittivity using applicable dielectric mixture theory.

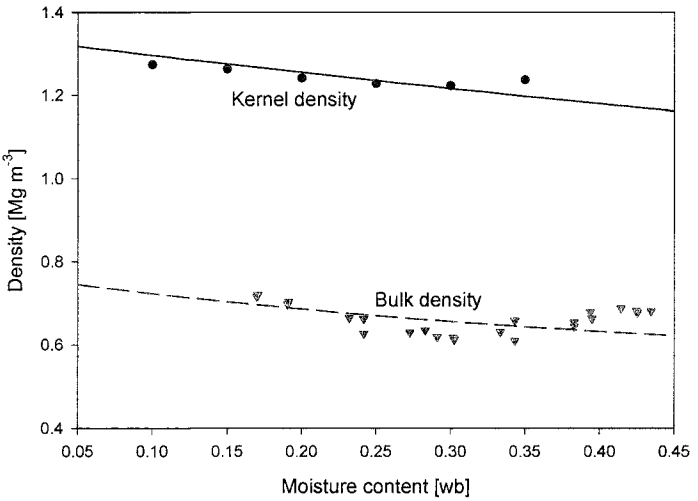

Fig. 4.8. Measured individual kernel [53] and bulk kernel densities [54] of field corn. Modeled results are obtained from Eq. (4.13) for kernel density (ρ_s = 1.34 Mg m^{-3}) and Eq. (4.15) for bulk density (k = 3, a/b = 2)

4.3.6 Constituent-Phase Configuration Influence on Bulk Permittivity

Friedman (1998) demonstrated the influence of constituent-phase configuration on modeled permittivities for six unique configurations of a concentric spherical model similar to the illustration in Fig. 4.1. Among the six possible combinations, water, solid, air (WSA), SWA, and ASW cover the range of permittivities exhibited by a wide range of porous media. Equation (4.6) was used to plot the configuration-dependent permittivities shown in Fig. 4.9. The combination of ASW and SWA forms an envelope about the permittivity of common mineral soils represented by the Topp et al. (1980) equation. Reduced permittivities found in high surface area porous materials are more closely described by SWA and WSA configurations.

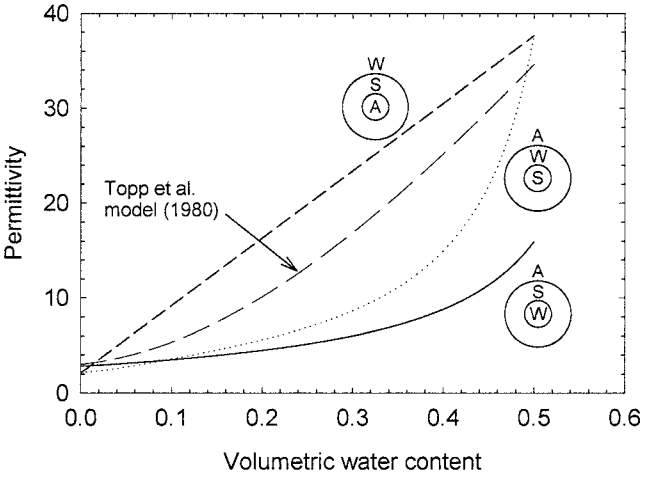

Fig. 4.9. Modeled permittivity of three different constituent-phase configurations where, for example, WSA represents water, solid and air with permittivities assuming modeled values of 80, 5, and 1, respectively. The Topp et al., 1980 expression describing mineral soils is shown for comparison

Swelling soils and plant seed constituents may expand, unfold and relax during drying and wetting, which for seeds may be accompanied by a change in shape and volume. Volume increases in soybean with hydration were found to be substantially greater than the weight of water imbibed, suggesting that polymeric seed constituents unfold with hydration [55]. We suggest this is a mechanism for increased surface area or evolving water-phase configuration. Evidence of this is seen in the sigmoidal shape of corn starch (Fig. 4.4c and d) and corn kernel (Fig. 4.10) moisture content-permittivity curves. Measured permittivities (200 MHz, [28]) of yellow-dent field corn kernels are shown in Fig. 4.10 where a combination of SWA and WSA could describe the complex water-solid configuration in cereal grains. A sigmoidal weighting distribution describes the relative contribution of SWA and WSA configurations shown in Fig. 4.10, which resulted in the modeled curve marked EMA. Such an approach was used successfully to model the three-phase system of moist soil combining configurations of ASW and SWA with an effective medium approximation (EMA) and estimates of bound water based on surface area [56]. Our justification for this approach is linked to kernel swelling or shrinking that occurs throughout the hierarchy of geometries contained in the starch grain. A second attempt to model the corn data was based on the surface area of the corn, which was increased 10 times at a critical water content to approximate a surface area increase for additional water binding (curve marked $A_s \times 10$). The effects of water binding in cereal grains and swelling soils are complicated by the volume change accompanied by wetting/drying processes and by the associated sample density changes.

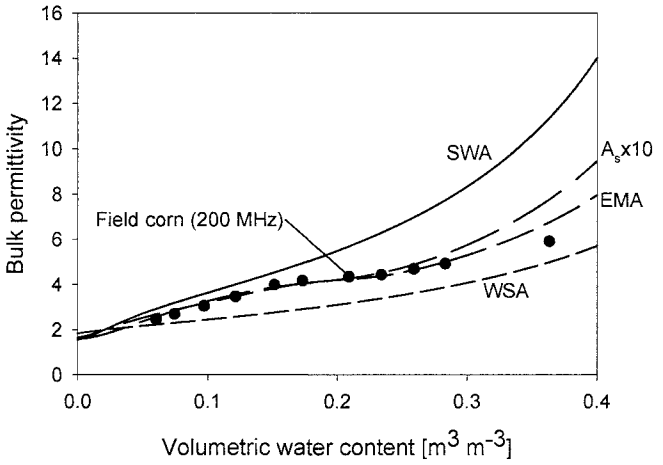

Fig. 4.10. Modeled permittivity of field corn using a sigmoidal increase in A_s (A_sx10) and using an effective medium approximation (EMA) of the two configurations, SWA and WSA with a sigmoidal increase in the WSA fraction with water content increase

4.4 Summary

Several factors influencing dielectric permittivity measurements in porous media have been identified using measurements and modeling approaches. Bound water associated with large surface area materials may lead to reduced dielectric, but other effects may also play a significant role in alteration of the permittivity-water content relationship. The thermodielectric effect observed in high surface area porous media might enhance or reduce the permittivity, depending on the water status and content and direction of temperature shift. Particle shape effects demonstrated in low-surface area media are a function of particle geometry and orientation with respect to the electrical field. In addition to bound water and geometrical effects, water-phase configuration may explain alteration of the bulk permittivity of wet porous media. Physical characteristics of porous media describe parameters critical for modeling permittivity, such as porosity and bulk density in addition to estimates of surface area. In general these can be broken down into representative estimates of solid, water and air fractions, with the volumetric water content being the variable of interest both for modeling purposes and for determination of water content from permittivity measurements. Identifying and separating bound water, particle shape and water-phase configuration effects in addition to other competing and perhaps confounding effects is an important step in understanding dielectric measurements in high surface area porous media for water content determination.

Acknowledgments

Partial funding for this work was provided by the Unites States-Israel Binational Agricultural Research and Development (BARD) Fund (Project IS-2839-97). We gratefully acknowledge research grants from Campbell Scientific and HarvestMaster (Logan, Utah) and Pioneer Hi-Bred International (Johnston, IA).

References

1. Topp GC, Davis JL, Annan AP (1980) Electromagnetic determination of soil water content: Measurements in coaxial transmission lines. Water Resour. Res. 16: 574-582
2. Sihvola A (1999) Electromagnetic mixing formulas and applications. Michael Faraday House, Stevenage, Herts, SG1 2AY, UK
3. Dasberg S, Dalton FN (1985) Time domain reflectometry field measurements of soil water content and electrical conductivity. Soil Sci. Soc. Am. J. 49: 293-297
4. Sihvola A, Lindell IV (1990) Polarizability and effective permittivity of layered and continuously inhomogeneous dielectric ellipsoids. J. Electromagn. Waves Appl. 4: 1-26
5. Jones SB, Friedman SP (2000) Particle shape effects on the effective permittivity of anisotropic or isotropic media consisting of aligned or randomly oriented ellipsoidal particles. Water Resour. Res. 36: 2821-2833
6. Kraszewski AW, Nelson SO (1996) In: Kraszewski A (ed) Microwave Aquametry. IEEE Press, NY, pp 177-203
7. Kelley JM, Stenoien JO, Isbell DE (1953) Wave-guide measurements in the microwave region on metal powders suspended in paraffin wax. J. Appl. Phys. 24: 258-262
8. Sillers RW (1936) The properties of a dielectric containing semi-conducting particles of various shapes. J. Inst. E.ect. Eng. 80: 378-394
9. Friedman SP, Robinson DA (2002) Particle shape characterization using angle of repose mesurements for predicting the effective permittivity and electrical conductivity of saturated granular media. Water Resour. Res. 38
10. Hillel D (1998) Environmental Soil Physics. Academic Press, San Diego
11. Brooker DB, Bakker-Arkema FW, Hall CW (1992) Drying and Storage of Grains and Oilseeds. Van Nostrand Reinhold, New York
12. Lamm G, Pack GR (1997) Local dielectric constants and Poisson-Boltzmann calculations of DNA counterion distributions. Int. J. Quant. Chem. 65: 1087-1093
13. Thorp JM (1959) The dielectric behaviour of vapours adsorbed on porous solids. Trans. Faraday Soc. 55: 442-454
14. Bockris JOM, Devanathan MAV, Muller K (1963) On the structure of charged interfaces. Proc. Roy. Soc. (London) A274: 55-79
15. Olhoeft GR (1981) In: Roy RF (ed) Physical Properties of Rocks and Minerals (CINDAS Data Series on Material Properties), vol II. McGraw-Hill, New York, pp 257-328
16. Nelson S, Lindroth D, Blake R (1989) Dielectric properties of selected and purified minerals at 1 to 22 GHz. J. Microwave Power Electromagnetic Energy. 24: 213-220
17. Booth F (1951) The dielectric constant of water and the saturation effect. J. Chem. Phys. 19: 391-394
18. Robinson DA, Jones SB, Wraith JM, Or D, Friedman SP (2003) A Review of Advances in Dielectric and Electrical Conductivity Measurement in Soils Using Time Domain Reflectometry. Vadose Zone J 2: 444-475

19. Oliver BM, Cage JM (1971) Electronic measurements and instrumentation. McGraw-Hill, New York
20. Weast RC (1986) CRC Handbook of Chemistry and Physics. CRC Press, Boca Raton, FL
21. Or D, Wraith JM (1999) Temperature effects on soil bulk dielectric permittivity measured by time domain reflectometry: A physical model. Water Resour. Res. 35: 371-383
22. Debye P (1929) Polar Molecules. Dover, Mineola, New York
23. Landau LD, Lifshitz EM (1960) Electrodynamics of Continuous Media. Permagon Press, New York
24. Schaap MG, deLange L, Heimovaara TJ (1996) TDR calibration of organic forest floor media. Soil Technology 11: 205-217
25. Jones SB, Or D (2002) Surface area, geometrical and configurational effects on permittivity of porous media. J. Non-Crystalline Solids. 305: 247-254
26. Dirksen C, Dasberg S (1993) Improved calibration of time domain reflectometry soil water content measurements. Soil Sci. Soc. Am. J. 57: 660-667
27. Ndife MK, Sumnu G, Bayindirli L (1998) Dielectric properties of six different species of starch at 2450 MHz. Food Research International. 31: 43-52
28. Jones RN, Bussey HE, Little WE, Mezker RF (1978). National Bureau of Standards, Boulder
29. Carter DL, Mortland MM, Kemper WE (1986) In: Klute A (ed) Methods of soil analysis, Part 1, Physical and mineralogical methods. ASA, Madison, WI, pp 413-423
30. Robinson DA, Cooper JD, Gardner CMK (2002) Modelling the relative permittivity of soils using soil hygroscopic water content. J. Hydrology. 255: 39-49
31. Leung HKH (1975) Capacity and force of water binding by carbohydrates and proteins as determined by nuclear magnetic resonance, Ph.D., University of Illinois at Urbana-Champaign
32. Leung HK, Steinberg MP, Wei LS, Nelson AI (1976) Water binding of macromolecules determined by pulsed NMR. J. Food Sci. 41: 297-300
33. Ryden BE (1992) In: Lund LJ (ed) Indirect methods for estimating the hydraulic properties of unsaturated soils. University of California Riverside, Riverside, CA, pp 693-706
34. Robinson RA, Stokes RH (1959) Electrolyte Solutions. Butterworths, London
35. Anderson DM, Low PF (1958) The density of water adsorbed by lithium-sodium- and potassium-bentonite. Soil Sci. Soc. Am. Proc. 22: 99-103
36. Low BW, Richards FM (1954) Measurements of the density, composition and related unit cell dimensions of some protein crystals. Am. Chem. Soc. J. 76: 2511-2518
37. Israelachvili JN (1992) Intermolecular and surface forces. Academic Press, San Diego
38. Gur-Arieh C, Nelson AI, Steinberg MP (1967) Studies on the density of water adsorbed on low-protein fraction of flour. J. Food Sci. 32: 442-445
39. Mackenzie RC (1958) Density of water sorbed on monmorillonite. Nature. 181: 334
40. Schoen M, Diestler DJ, Cushman JH (1987) Fluids in micropores. I. Structures of a simple classical fluid in a slit-pore. J. Chem. Phys. 87: 5464-5476
41. Agmon N (1996) Tetrahedral displacement: The molecular mechanism behind the Debye relaxation in water. J. Phys. Chem. 100: 1072-1080
42. Ratkovic S, Pissis P (1997) Water binding to biopolymers in different cereals and legumes: Proton NMR relaxation, dielectric and water imbibition studies. J. Material Sci. 32: 3061-3068
43. Konsta AA, Pissis P, Kanapitsas A, Ratkovic S (1996) Dielectric and conductivity studies of the hydration mechanisms in plant seeds. Biophysical Journal. 70: 1485-1493

44. Leschansky YI, Lebedeva GN, Shumilin VD (1971) Electrical parameters of sandy and loamy grounds in the range of centimeter, decimeter, and meter wavelength. Izv. Vyss. Ucheb. Zaved. Radiofiz. 14: 562-569
45. Thies-Weesie DME, Philipse AP, Kluijtmans SGIM (1995) Preparation of sterically stabilized silica-hematite ellipsoids: Sedimentation, permeation, and packing properties of prolate colloids. J. Colloid Interface Sci. 174: 211-223
46. Cumberland DJ, Crawford R (1987) In: Allen T (ed) Handbook of Powder Technology, vol 6. Elsevier, Amsterdam
47. Sokhansanj S, Lang W (1996) Prediction of kernel and bulk volume of wheat and canola during adsorption and desorption. J. Agric. Engng. Res. 63: 129-136
48. Milewski JV (1978) The combined packing of rods and spheres in reinforcing plastics. Ind. Eng. Chem. Prod. Res. Dev. 17
49. Mohsenin NN (1970) Physical properties of plant and animal materials: Structure, physical characteristics and mechanical properties. Gordon and Breach Science Publishers, New York
50. Sokhansanj S, Falacinski AA, Sosulski FW, Jayas DS, Tang J (1990) Resistance of bulk lentils to airflow. Trans. ASAE. 33: 1281-1285
51. Cherkaeva E, Golden KM (1998) Inverse bounds for microstructural parameters of composite media derived from complex permittivity measurements. Waves in Random Media 8: 437-450
52. Trabelsi S, Nelson SO (1998) Density-independent function for on-line microwave moisture meters: a general discussion. Meas. Sci. and Tech. 9: 570-578
53. Nelson SO (1979) RF and microwave dielectric properties of shelled, yellow-dent field corn. Trans. ASAE. 22: 1451-1457
54. Brusewitz GH (1975) Density of rewetted high moisture grains. Trans. ASAE 18: 935-938
55. Leopold AC (1983) Volumetric components of seed imbibition. Plant Physiol. 73: 677
56. Friedman SP (1998) A saturation degree-dependent composite spheres model for describing the effective dielectric constant of unsaturated porous media. Water Resour. Res. 34: 2949-2961